

Dense fluid transport through nanoporous graphene membranes in the limit of steric exclusion

Runfeng Zhou ^{1,2} Mathew M. Swisher ^{1,3} Akshay Deshmukh ¹ Chengzhen Sun ²
John H. Lienhard ¹ and Nicolas G. Hadjiconstantinou^{1,3,*}

¹*Department of Mechanical Engineering, Massachusetts Institute of Technology, Cambridge, Massachusetts 02139, USA*

²*State Key Laboratory of Multiphase Flow in Power Engineering, Xi'an Jiaotong University, Xi'an, Shaanxi 710049, China*

³*Center for Computational Science & Engineering, Massachusetts Institute of Technology, Cambridge, Massachusetts 02139, USA*



(Received 6 December 2023; accepted 6 March 2024; published 9 April 2024)

We investigate transport of dense fluid flow through nanoporous membranes in the limit of steric exclusion using molecular dynamics (MD) and finite element simulations. Simulation results suggest that, for simple fluids, deviations from Sampson flow are a consequence of the competition between slip and finite atomic size effects. The latter manifest themselves by introducing an effective pore size, as well as an effective membrane thickness. We propose an analytical model for the membrane permeance that accounts for all these factors. We also show how this model can be modified to describe transport of low molecular weight aromatic hydrocarbons across these membranes in the steric limit. Extensive validation of this model is conducted through MD simulations of Lennard-Jones fluids permeating single- and multilayer graphene membranes, as well as low molecular weight organic liquids permeating single-layer graphene membranes.

DOI: [10.1103/PhysRevFluids.9.044202](https://doi.org/10.1103/PhysRevFluids.9.044202)

I. INTRODUCTION

By avoiding the energy-intensive vapor-liquid phase change, membrane-based processes have the potential to drastically reduce the energy consumption of many key chemical separations [1–4]. Nanoporous graphene membranes, which combine minimal flow resistance with high mechanical strength and chemical stability, have the potential to revolutionize tough separations ranging from gas separation to organic solvent reverse osmosis and nanofiltration [5–13]. Understanding how molecular and pore geometry impact membrane permeance and selectivity is critical for future membrane and process design. Potential large-scale application of such membranes makes accurate prediction of their permeability very important [14,15] for their design, as well as the design and optimization of large-scale separation systems utilizing them [16–20].

In contrast to dilute gases in which the diffusive transport closure and concomitant Navier-Stokes description is replaced by transitional and ultimately ballistic transport as length scales decrease [21,22], in dense fluid flows the Navier-Stokes description, aided by slip-flow corrections, remains remarkably robust even at length scales as small as a few nanometers [23,24]. For sufficiently thin membranes, the Navier-Stokes description for the fluid permeance is given by Sampson's solution

*ngh@mit.edu

[25] of the Stokes equation for infinitely thin membranes,

$$\frac{Q}{\Delta P} = \frac{R^3}{3\mu}, \quad (1)$$

where Q denotes the flowrate, ΔP the pressure difference across the membrane, R is the nominal pore radius, and μ the fluid viscosity. However, studies of flow through a single-layer nanoporous graphene membranes reported deviations compared to the predictions of the Sampson equation [26–33]. These deviations were attributed to a number of small-scale phenomena, such as slip and reduced mobility due to fluid layering at the fluid-membrane interface, leading to a number of empirical modifications to Eq. (1).

In this paper we perform molecular dynamics (MD) and finite element (FE) simulations to investigate the flow of simple dense fluids as well as low molecular weight hydrocarbon liquids across nanoporous membranes. Our investigation shows that for simple liquids the observed behavior is a result of the competition between slip and finite atomic size effects [27,34]. The latter manifests itself in regularizing the infinitely thin membrane to finite thickness, as well as defining an effective pore size available for transport [27,30]. We note that our simulation results also suggest that no modifications to the fluid constitutive relation (e.g., scale-dependent viscosity) are necessary. This can be motivated by noting that the primary source of flow resistance in Sampson-type flows is geometric [27].

Taking these observations into consideration, in Sec. II we propose an analytical Navier-Stokes-based model for describing the membrane permeance. This model is extensively validated in Sec. III using MD simulations of Lennard-Jones (LJ) fluids for single- as well as multilayer graphene membranes. In Sec. IV we additionally show that the proposed model can be used to describe the permeance of low molecular weight organic liquids through single-layer graphene membranes. In the case of aromatic hydrocarbons in particular, the model can be modified to provide accurate descriptions of flow rates for very small pores, including near the steric exclusion limit.

II. PERMEANCE MODEL

In this section we develop a model for describing the permeance of dense fluids across single-layer nanoporous membranes. By choice and subject to validation—see Sec. III below for results and further discussion—our model will account for the finite thickness of the single-layer membrane by modifying the Sampson component of the flow resistance. In other words, as shown in Fig. 1(a), a single-layer membrane of nominal radius R , effective radius $R - \delta$ and thickness 2δ , where δ denotes the characteristic size of the excluded volume associated with one atomic layer, will be modeled as a membrane of thickness $L = 0$ and radius $R - \delta$ via modification of Eq. (1); see Appendix A for the definition of the nominal radius from an atomistic point of view. Multilayer membranes will be discussed in Sec. III C.

A. Finite element simulations

The modifications to Eq. (1) will be informed by FE simulations of the flow through these membranes. We specifically considered two model geometries [see Fig. 1(b)]: domain I corresponds to an ideal membrane with a nominal radius of R and effective pore radius of $R - \delta$; domain II takes into account that for graphene membranes functional groups with characteristic sizes slightly smaller than carbon atoms, such as hydrogen atoms, are often grafted onto the edges of pores. To mimic more realistic pores, in domain II we take the membrane’s thickness away from the pore to be 2.4δ without changing the geometry near the pore. All FE simulations were conducted using the COMSOL MULTIPHYSICS software. A mesh independence study was performed to ensure the reliability and accuracy of the simulation results.

Figure 1(c) summarizes the FE results for the reduced fluid permeance ($\frac{Q}{\Delta P} \cdot \frac{3\mu}{R^3}$) as a function of the reduced radius ($\tilde{R}_\delta \equiv \frac{R-\delta}{R} = 1 - \frac{\delta}{R}$). In particular, the figure shows two results, which bound the

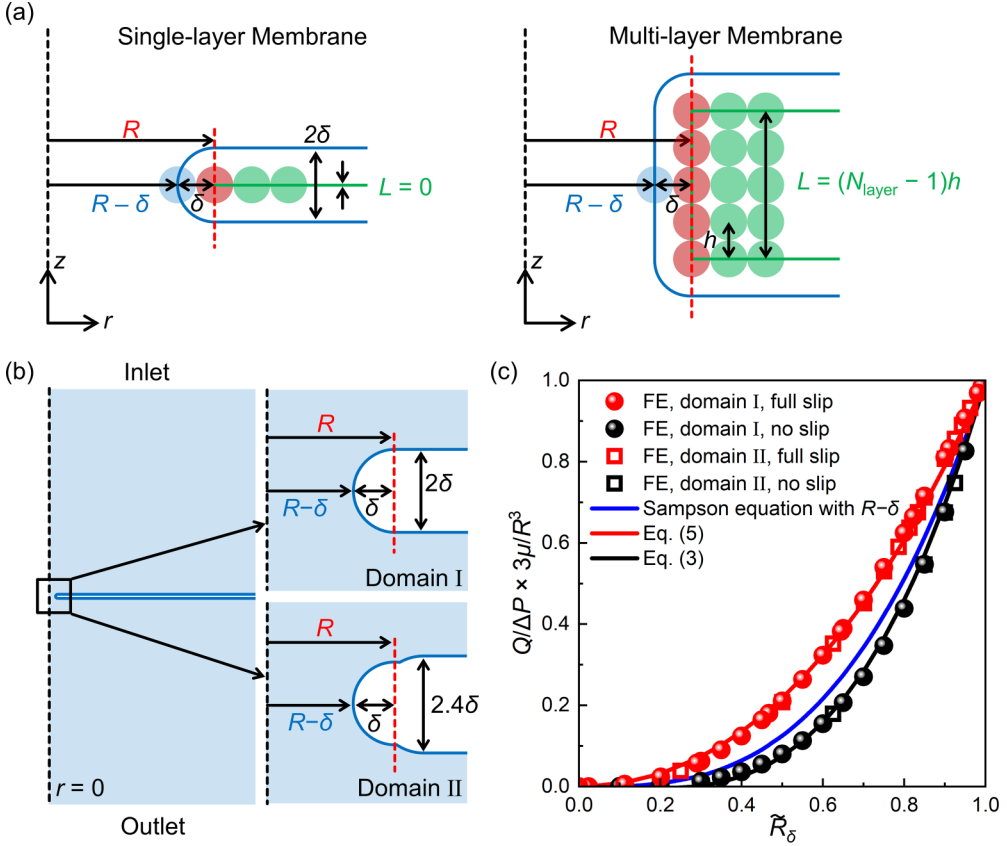


FIG. 1. Membrane geometry and FE calculations for the permeance across a single-layer membrane. (a) Model geometry for single-layer and multilayer membranes. Left: Single-layer membrane; right: multilayer membrane. Fluid atoms are shown in blue, atoms at the edge of the pore (functionalization) in red and atoms on the membrane in green. The blue line represents the boundary that fluid atoms can reach. L represents the respective membrane width (pore length) for use in model (9). (b) Computational domains for FE calculations. The membrane surface is denoted by a blue line. (c) FE results for the reduced permeance as a function of reduced radius. Blue line corresponds to Sampson result for a pore of radius $R - \delta$. Red dots and hollow squares denote FE results for the full-slip case with domain I and domain II, respectively, while the solid curved line denotes the approximate model given by Eq. (5). Black dots and hollow squares denote FE results for the no slip case with domain I and domain II, respectively, while the solid line denotes the approximate model given by Eq. (3).

effect of slip on this system. The lower bound corresponds to the case of no slip along the membrane surface. The upper bound corresponds to the case of full slip along the membrane surface. These two cases envelope the Sampson permeance for a membrane of zero thickness and radius $R - \delta$. Additionally, we find that the difference in reduced fluid permeance between domain I and domain II calculations is very small, which indicates that the resistance of the porous membrane is sensitive only to the geometric structure near the pore edges while not sensitive to small changes to the thickness profile of the membrane. Therefore, in the interest of simplicity, the ensuing discussion is based on the results obtained from domain I.

These results show that, compared to infinitely thin membranes, membrane thickness due to the finite atomic size increases flow resistance. However, the presence of slip effects can compensate for this additional resistance, resulting in actual permeance higher than those predicted by the Sampson

equation with a radius of $R - \delta$; these observations are in agreement with previous work [27,29,30]. In this work, we will use MD simulation results to guide the choice between these two limiting cases.

B. Analytical expressions for the FE results

The FE results discussed above and summarized in Fig. 1 can be described to a good approximation level using modifications of the standard Sampson expression [Eq. (1)]. In this development we make the assumption $\delta \ll R$, which is satisfied for the majority of pores considered here and is expected to be a reasonable approximation for systems described by the Navier-Stokes equation (consistent with the use of a FE model).

Starting with the no-slip case, we note that the flow resistance can be approximated using the Dagan model [35], namely as a combination of a Sampson and Poiseuille components

$$\frac{\Delta P}{Q} = \frac{3\mu}{(R - \delta)^3} + \frac{8\mu C_1 2\delta}{\pi(R - \delta)^4}, \quad (2)$$

where $C_1 > 0$ represents a correction for the curved pore entrance (in contrast to the Dagan case featuring a step entrance). Collecting terms and using the assumption $\delta \ll R$ we obtain the following result for the permeance:

$$\frac{Q}{\Delta P} = \frac{(R - \delta)^3}{3\mu} \left[1 - \frac{16C_1\delta}{3\pi(R - \delta)} \right]. \quad (3)$$

The full-slip case can be brought into an expression of similar form. Assuming that in this case dissipation due to the curved part of the pore is negligible [27] we write the permeance in the form

$$\frac{Q}{\Delta P} = \frac{(R - \alpha\delta)^3}{3\mu}, \quad (4)$$

where $0 < \alpha < 1$ accounts for the fact that due to the curved pore entrance, the effective pore radius lies between R and $R - \delta$. Using the assumption $\delta \ll R$, the above expression can be written in the form

$$\frac{Q}{\Delta P} = \frac{(R - \delta)^3}{3\mu} \left[1 + \frac{3(1 - \alpha)\delta}{R - \delta} \right]. \quad (5)$$

As shown in Fig. 1(c), expression (3) with $C_1 = 0.24$ and expression (5) with $\alpha = 0.75$ provide good approximations to the corresponding FE results for $\frac{\delta}{R} < 0.5$, which extends beyond the expected range of validity predicted by our original assumption that $\delta \ll R$. We also note that the two models are both of the form

$$\frac{Q}{\Delta P} = \frac{(R - \delta)^3}{3\mu} \left(1 + \frac{\beta}{R - \delta} \right), \quad (6)$$

where β can be regarded as an effective slip length, which resembles the slip-corrected Sampson equation

$$\frac{Q}{\Delta P} = \frac{a^3}{3\mu} \left(1 + \frac{\beta}{a} \right) \quad (7)$$

employed previously [26,31] (and [30] following linearization) to describe MD simulation data, where a , here, denotes some effective pore radius.

III. VALIDATION

In this section we present extensive validation of the model presented in Sec. II using MD simulations.

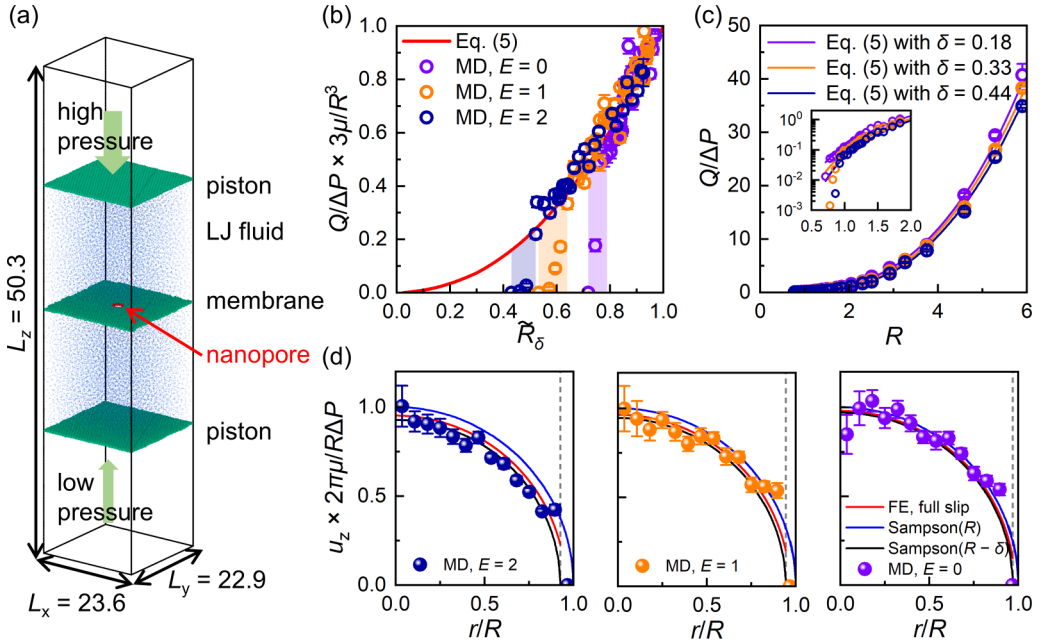


FIG. 2. MD simulation results. (a) MD simulation geometry. Carbon atoms on graphene membrane shown in green, hydrogen atoms in red, and LJ fluid shown in blue dots. (b) Reduced permeance in MD simulations as a function of reduced radius with δ chosen as discussed in the text. Circles denote MD results. The red solid line denotes the full-slip model given by Eq. (5). The shaded regions show the range of values of \tilde{R}_δ for each fluid over which the permeance reduces to zero due to steric effects. (c) Lennard-Jones fluid permeance as a function of nominal radius. Circles denote the MD results. Solid lines denote the full-slip model given by Eq. (5) with corresponding δ . Inset: Details of permeance in the small pores. (d) Normalized axial flow velocity as a function of radius for $R = 5.9$. Circles represent MD simulation results with error bars determined based on the standard error. Red solid lines correspond to additional FE simulation results with $R = 5.9$ and δ as determined for the comparisons in (b) and (c) (see text for details). Blue solid lines correspond to Sampson's velocity profile for a pore of radius R [Eq. (8)]. Black solid lines correspond to Sampson's velocity profile for a pore of radius $R - \delta$. The vertical gray dashed line represents $R - \delta$.

A. Validation using MD simulations

In the sections that follow, we use MD simulation results of dense LJ fluid flow through nanoporous graphene to validate the model proposed in the previous section. The simulation system is shown in Fig. 2(a) and more details can be found in Appendix A. The comparisons extend over the three fluid-solid interaction strengths considered in this work, denoted here by $E = \{0, 1, 2\}$ in order of increasing interaction strength. As expected, the fluid-solid interaction strengths will have an effect on δ , which is the only free parameter in this model. In what follows we discuss how δ was determined for each value of fluid-solid interaction.

The amount of slip present on the graphene surface will have an effect on the permeance, as exemplified by the two limiting cases discussed in Fig. 1(c). Given the large slip typically associated with the graphene surface [36–43], we proceed by using the full-slip model [Eq. (5)] to fit our MD data. We determine the effective slip length from the relation $\beta = 3(1 - \alpha)\delta = 0.75\delta$, where $\alpha = 0.75$ has been determined from fitting the full-slip FE simulation results of Fig. 1(c) using Eq. (5).

In the comparisons of Fig. 2, δ was taken to have the values $\{0.18, 0.33, 0.44\}$ corresponding to $E = \{0, 1, 2\}$, respectively; corresponding values of β are $\{0.14, 0.25, 0.33\}$. These δ values were chosen as the ones yielding best agreement between the model (5) and MD simulation results. Here

TABLE I. Estimates of critical radius at which permeance drops off from theoretical predictions as a function of fluid-solid interaction. As explained in text, the values reported here are based on the radius at which the permeance starts to deviate from model (5). All three results are consistent with $R_{\text{crit}} \approx \sigma_{\text{hf}} = 0.84$.

Interaction strength	δ	$(\tilde{R}_\delta)_{\text{crit}}$	R_{crit}
$E = 0$	0.18	0.78	0.81
$E = 1$	0.33	0.63	0.88
$E = 2$	0.44	0.52	0.92

we note that these values are somewhat smaller than the nominal minimum approach distances reported in other studies [34,44]. This can be motivated by the following two observations: first, fluid atoms are primarily repelled by the ring of hydrogen atoms terminating the pore and thus that repulsion distance will scale with $\sigma_{\text{hf}} = 0.84 < \sigma_{\text{cf}} = 1$; second, due to the pore geometry, the line density of hydrogen atoms terminating the pore is quite small leading to smaller overall repulsion and closer approach distances compared to a solid wall. We also note that as a measure of pore-radius reduction for flow rate purposes, δ will be somewhat different from the minimum approach distance calculated in Refs. [34,44], since the former also takes into account, in an aggregate sense, density nonuniformity effects that affect the mass flux through the pore.

Figure 2(b) shows good agreement between MD results and FE simulations, with the MD results collapsing onto the full-slip FE results, with the exception of data for which $\tilde{R}_\delta < (\tilde{R}_\delta)_{\text{crit}}$, where $(\tilde{R}_\delta)_{\text{crit}}$ denotes a critical reduced radius at which drop off in permeance due to steric interactions is first observed. We emphasize that the value of δ is fixed for each pair of fluid-solid interactions, that is, δ is not adjusted as a function of the pore radius.

Based on the data of Fig. 2(b), we estimate $(\tilde{R}_\delta)_{\text{crit}} = 0.78, 0.63, 0.52$ for $E = 0, 1, 2$, respectively. Table I shows the resulting critical radii calculated using the known values of δ as a function of E . We observe that $R_{\text{crit}} \approx \sigma_{\text{hf}}$ for all three values of E , which is consistent with the physical interpretation of the model. We also note that due to the finite range of values of \tilde{R}_δ over which the permeance drops off, we could have defined $(\tilde{R}_\delta)_{\text{crit}}$ as the critical reduced radius at which the permeance has reduced to zero. Our measurements suggest that this definition leads to $R_{\text{crit}} \approx 0.8\sigma_{\text{hf}}$ (averaged over the three values of E).

We also note that the relationship between β and fluid-solid interactions runs counter to expectation, as one would typically expect weaker fluid-solid interactions to correspond to larger slip lengths [24,37,45]. This can be explained by noting that, although appearing as an effective slip coefficient in Eq. (6), variations in β do not necessarily reflect changes in the amount of slip at the fluid-solid interface. In fact, the FE simulations on which model (5) is based assumed large, constant slip. More precisely, the values of β reported here are a result of direct application of relation $\beta = 0.75\delta$: weak fluid-solid interactions result in a smaller δ , which in turn leads to a smaller β .

1. Membrane permeance

Figure 2(c) shows the permeance of the LJ fluid, $Q/\Delta P$, as a function of the nominal pore radius, R . Although equivalent to the information presented in Fig. 2(b), the present form serves to highlight the dependence of the permeance on physical quantities of interest, such as the nominal pore radius and the fluid-solid interaction strength. For reference, the prediction based on Eq. (5) is also included in Fig. 2(c). The simulation results align very well with the model developed here. As shown in the inset of Fig. 2(c) and Table I, the agreement extends to pores with radii approaching the steric limit for which the continuum description is not normally expected to hold.

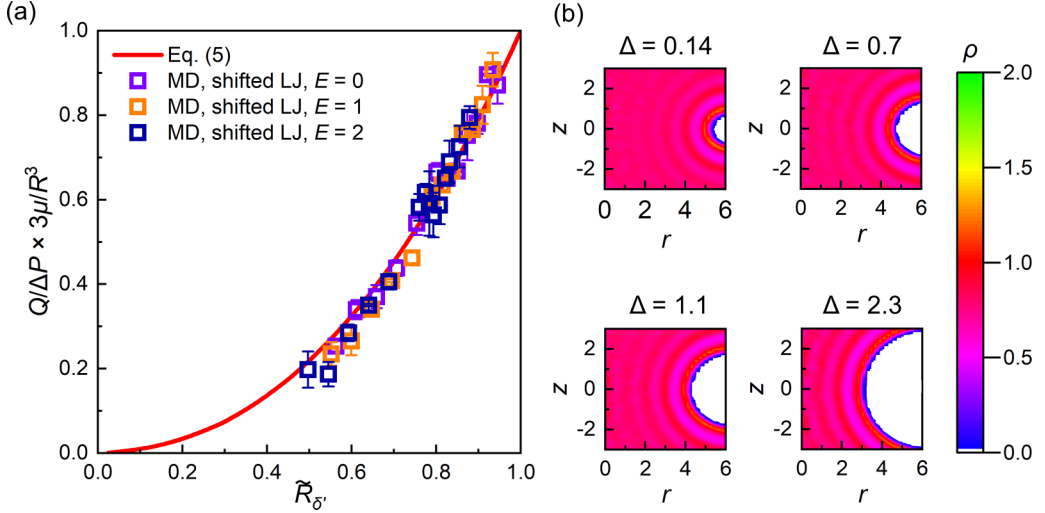


FIG. 3. Simulation results using the shifted LJ potential (13). (a) Reduced permeance as a function of $\tilde{R}_{\delta'}$ from MD simulations using the shifted potential. (b) Density distribution near the pore for varied shift parameter Δ .

2. Velocity profile in the pore

Figure 2(d) compares the velocity profiles from MD simulations, FE simulations, and those derived from the Sampson result

$$u_z(r) = \frac{R\Delta P}{2\pi\mu} \sqrt{1 - \frac{r^2}{R^2}}. \quad (8)$$

The latter is shown for a radius of R and $R - \delta$, normalized by $\frac{R\Delta P}{2\pi\mu}$ in both cases.

The comparison shows that the Sampson velocity profile based on the nominal radius (R) does not describe the MD data, as expected. In contrast, the velocity profile obtained from the FE simulation is in good agreement with the MD data given the statistical uncertainty in the latter. The figure also shows that the FE flow field (and thus the MD data) can be approximated reasonably well by the Sampson profile (8) provided the radius is replaced by the effective radius $R - \delta$. This is to be expected since the two differ only by the effective slip term $\frac{\beta}{R-\delta}$ in (5), where $\beta \propto \delta$. The figure highlights this by comparing the three values of fluid-solid interaction; as the fluid-solid interaction increases, δ increases and the discrepancy between the two profiles increases.

B. Validation of effective radius results using a shifted LJ potential

Parameter δ , which is central to model (5), is physically interpreted as a measure of the excluded volume associated with the fluid-solid atomic interaction. In this section we present results of a simulation experiment devised to test the consistency of this physical interpretation and thus provide further validation for the model presented in this paper.

The experiment is based on the hypothesis that, with all other system parameters remaining unchanged, a change in the size of the repulsive core of the solid-fluid interaction potential should translate directly to an equivalent change in this excluded volume. More precisely, we would expect that an increase in the repulsive core size by Δ would lead to an excluded size of magnitude $\delta' = \Delta + \delta$ and therefore, in the presence of no other change, the MD data would follow the FE results of Fig. 1(c) (or equivalently model 5) if plotted versus $\tilde{R}_{\delta'} = 1 - \frac{\delta'}{R}$.

Figure 3(a) shows the result from a set of MD simulations designed to test this hypothesis for a pore of size $R = 5.9$ and $0 \leq \Delta \leq 2.3$. These simulations used the modified LJ potential (13) to describe the interactions between hydrogen atoms and fluid atoms, as well as those between carbon atoms and fluid atoms to maintain the membrane structure.

The permeance data was analyzed as follows. For each value of E we used a least-squares fit to find the value of δ such that MD data align with the full-slip FE simulation results, as in the case of model (5). This fitting procedure returned $\delta = 0.28, 0.32, 0.66$, for $E = 0, 1, 2$, respectively. The dependence of δ on fluid-solid interaction strength observed here is consistent with that obtained in the previous section, although actual values are slightly different. Figure 3(b) illustrates the growth in excluded volume as Δ increases via direct observation of the fluid density distribution in the pore vicinity.

Here we note that the value of δ determined as discussed above corresponds to a horizontal shift and has clearly no effect on the slope of the MD data as a function of R_{δ} , which is seen to be in good agreement with model (5). This independent test validates the physical interpretation of our model and parameter δ in particular and also suggests that potential additional effects not captured by our model are small.

C. Validation using multilayer membranes

In this section we consider the permeance of multilayer membranes as additional validation for the model (5). The resistance $\mathcal{R} \equiv \frac{\Delta P}{Q}$ of a multilayer membrane can be treated using Dagan's result [35]

$$\mathcal{R} = \frac{3\mu}{(R - \delta)^3} \left(1 + \frac{\beta}{R - \delta}\right)^{-1} + \frac{8\mu L}{\pi(R - \delta)^4} \left(1 + \frac{4l_s}{R - \delta}\right)^{-1}, \quad (9)$$

where the additional resistance due to the membrane thickness is accounted for using a Poiseuille flow component; here, L denotes the length of the pore and l_s denotes the slip length inside the pore. We note in particular that as an extension of model (5), L in Eq. (9) does not include the thickness of the first layer, since the latter has already been taken into account in the single-layer model. In other words, $L = (N_{\text{layer}} - 1)h$, where N_{layer} denotes the number of layers and $h = \sigma_{\text{cc}}$ is the interlayer spacing, as illustrated in Fig. 1(a).

To validate this model, we conducted MD simulations of flow through multilayer membranes with varying numbers of layers $N_{\text{layer}} = 1-13$ using three different pore sizes: a large-sized pore ($R = 5.9$), a medium-sized pore ($R = 2.5$), and a small-sized pore ($R = 1.6$). The fluid-solid interaction strength was set to $E = 2$.

Figure 4 illustrates that the variation in resistance aligns with expectations. The simulation results are in good agreement with the predictions from Eq. (9), with a fitted slip length $l_s = 0.14$. To further validate these results, we increase the interaction strength between hydrogen atoms and the fluid within the medium-sized pore to mimic a pore wall with strong friction. The simulation results, summarized in the inset of Fig. 4, exhibit increased flow resistance, which can be accurately described by substituting $l_s = 0$ into the Poiseuille term in Eq. (9).

IV. APPLICATION TO PERMEATION OF LOW MOLECULAR WEIGHT ORGANIC LIQUIDS

In this section we further validate model (5), by assessing its ability to accurately describe MD simulation results for the permeance of low-molecular weight organic liquids. Given the more realistic application considered here, we will be using the CHARMM force field [46] to model this system. Simulation details can be found in Appendix B. We specifically consider aromatic hydrocarbons with a planar benzene ring structure, such as *o*-xylene, *p*-xylene, and benzene, as well as aliphatic hydrocarbons with a chain structure such as *n*-octane and *i*-octane. The molecular structures are depicted in Fig. 5(a). As remarked in Sec. I, theoretical descriptions of permeation rates for these substances are of great importance for separation applications [18].

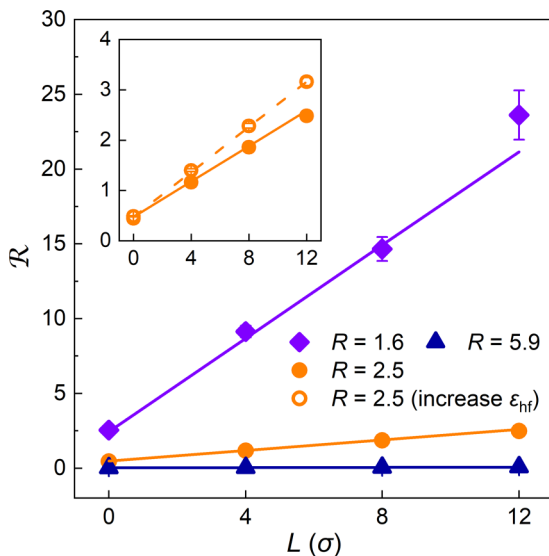


FIG. 4. Flow resistance in LJ units as a function of membrane thickness obtained from MD simulations for three different pore sizes. Solid lines denote model given by Eq. (9) with $l_s = 0.14$. Inset: Change in resistance due to stronger fluid-solid interactions in a medium-sized pore; dashed line denotes model given by Eq. (9) with $l_s = 0$.

A. Simulation results and comparison with the model

A comparison between simulation results and the model given by Eq. (5) is presented in Fig. 5(b). Given the use of this more realistic potential, results in this section will be reported in SI units. In this comparison δ was treated as a fitting parameter, leading to $\delta = 1.64, 1.45, 1.26, 1.65, 2.09 \text{ \AA}$ for *o*-xylene, *p*-xylene, benzene, *n*-octane, and *i*-octane, respectively. We observe that in all cases

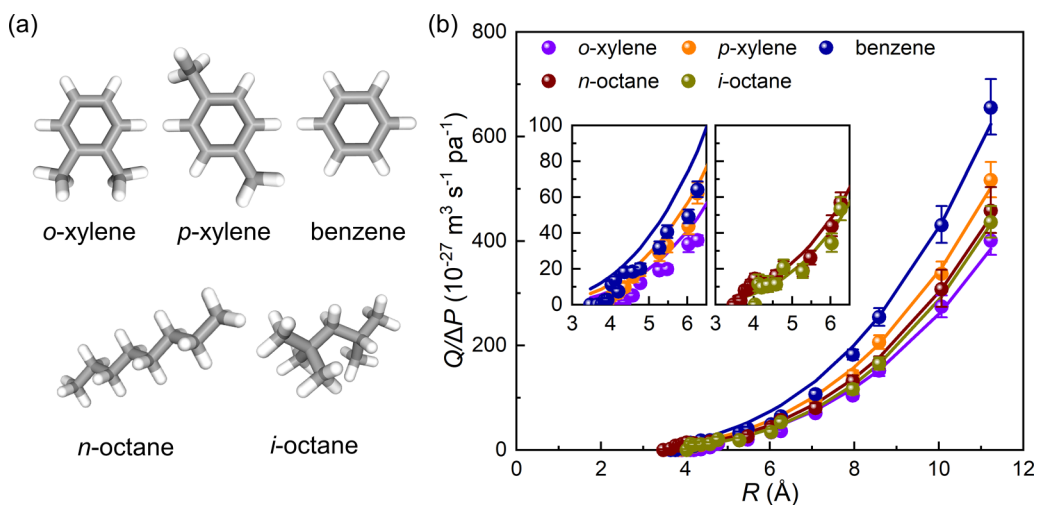


FIG. 5. (a) Molecular structure [47] and (b) permeance of *o*-xylene, *p*-xylene, benzene, *n*-octane, and *i*-octane. Circles denote MD results. Solid lines denote model given by Eq. (5). Inset in (b) shows detailed comparison for small pores.

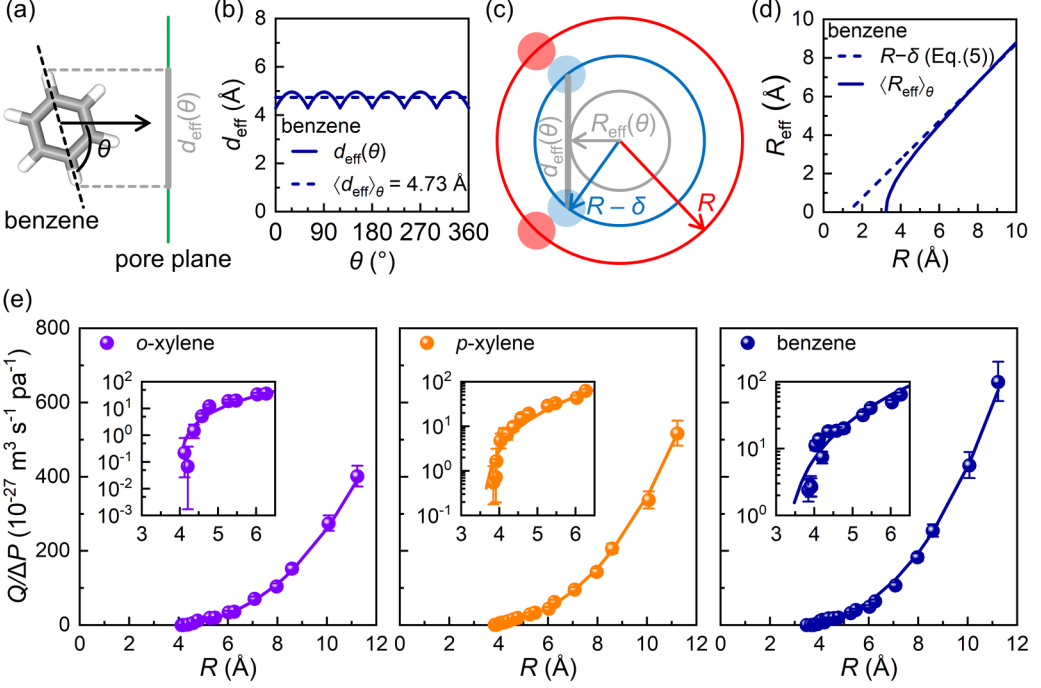


FIG. 6. Effective radius and extended permeance model for aromatic liquids. (a) Definition of characteristic width $d_{\text{eff}}(\theta)$ and (b) its variation with θ for benzene. (c) Schematic of effective radius R_{eff} for aromatic liquids, where red and blue dots represent the hydrogen atoms at the edge of the pore and end of the aromatic molecules, respectively. (d) R_{eff} for benzene. (e) Permeance of *o*-xylene, *p*-xylene, and benzene; circles denote MD results; solid lines denote extended model given by Eq. (10) with $R_{\text{eff}} = \langle R_{\text{eff}} \rangle_{\theta}$ as given by Eq. (11).

the model is able to capture the permeance of these fluids despite their more complex molecular structure. For aliphatic hydrocarbons, the model remains effective even as the radii approach the steric limit, similar to LJ fluids, but for aromatic hydrocarbons, theoretical predictions exceed simulation values at small pore sizes [see insets in Fig. 5(b)]. In the next section, we will consider the unique structure of aromatic hydrocarbons to further extend this model.

B. Steric considerations: Further extended model

Given the recent interest in separation by size exclusion [1], in this section we discuss how the model given by Eq. (5) can be extended to incorporate some information about molecular structure and thus approximately capture the liquid permeance close to the limit of steric exclusion. As discussed below, the modifications discussed here are limited to the planar aromatic hydrocarbons considered above, namely *o*-xylene, *p*-xylene, and benzene.

The essence of the proposed modification for these hydrocarbon molecules stems from the observation that, as a result of their molecular size, their center of mass cannot reach the pore edge, requiring the introduction of a more general effective pore radius R_{eff} . In other words, we seek to describe the permeance by a more general form of (5) given by

$$\frac{Q}{\Delta P} = \frac{R_{\text{eff}}^3}{3\mu} \left(1 + \frac{\beta}{R_{\text{eff}}} \right), \quad (10)$$

where $\beta = 0.75\delta$ and $R_{\text{eff}} \rightarrow R - \delta$ as the liquid molecule approaches a LJ sphere.

As shown in Figs. 6(a)–6(d), this effective radius can be defined relatively straightforwardly for planar aromatic hydrocarbons, under the assumption that molecules entering the pore at its edge do so with their molecular plane at right angles to the pore plane. For each value of θ as defined in Fig. 6(a), one may define an effective radius $R_{\text{eff}}(\theta)$ as the radius of the circular pore that will allow permeation of the molecule in the assumed configuration. In other words, $R_{\text{eff}}(\theta) = \sqrt{(R - \delta)^2 - \left(\frac{d_{\text{eff}}(\theta)}{2}\right)^2}$, where $d_{\text{eff}}(\theta)$ denotes the θ -dependent cord length the molecules project on the plane of the pore [see Figs. 6(a)–6(c)]. In the interest of simplicity, here we approximate the effective radius averaged over all θ by the expression

$$\langle R_{\text{eff}} \rangle_{\theta} = \sqrt{(R - \delta)^2 - \left(\frac{\langle d_{\text{eff}} \rangle_{\theta}}{2}\right)^2}, \quad (11)$$

where $\langle \cdot \rangle_{\theta}$ denotes averaging over all θ . The above approximation is reasonable because the amplitude of the variation in $d_{\text{eff}}(\theta)$ is relatively small [see Fig. 6(b)].

By interpolating between the values of δ obtained from the LJ simulation we estimate $\delta \approx 0.84 \text{ \AA}$ for aromatic hydrocarbons. We note that this value is smaller than the value used in Fig. 5. This can be motivated by noting that, here, δ represents only the exclusion volume of hydrogen atoms—specifically, hydrogen atoms on the organic molecules interacting with hydrogen atoms at the pore edge—while as used in the results of Fig. 5, δ represents the exclusion volume of the entire organic molecule.

The characteristic length $\langle d_{\text{eff}} \rangle_{\theta}$ is determined through a best fit with the MD permeance data, resulting in the values 6.26, 5.41, 4.68 \AA for *o*-xylene, *p*-xylene, and benzene, respectively. If we assume that the benzene molecule adopts all angles with equal probability due to the high symmetry of the benzene ring, using the dependence of d_{eff} on θ shown in Fig. 6(b), direct calculation yields $\langle d_{\text{eff}} \rangle_{\theta} = 4.73 \text{ \AA}$, which is consistent with the fitted result. Repeating the calculation for the other molecules results in similarly consistent results, although the lack of symmetry tends to introduce slightly worse agreement than this case. These findings highlight the robustness of our approach and the reliability of the assumptions made in our analysis.

Figure 6(d) shows the variation of the effective pore radius R_{eff} for benzene as a function of the nominal pore radius R . As expected, the effective pore radius $R_{\text{eff}} = \langle R_{\text{eff}} \rangle_{\theta}$ diverges from the LJ value $R - \delta$ and decreases rapidly to zero as the nominal pore radius becomes small.

A comparison between simulation results and the extended model given by Eq. (10) with $R_{\text{eff}} = \langle R_{\text{eff}} \rangle_{\theta}$ as given by Eq. (11) is presented in Fig. 6(e). Despite the number of approximations introduced, the agreement between the MD data and the extended model is very good for all pore radii including in the steric limit. Given the purely geometric nature of the effective pore radius model developed here, the agreement between the MD data and model (10) highlights the robustness of the continuum description at small scales.

V. CONCLUSIONS

We have developed a hydrodynamic model for predicting the flow of simple fluids through single- and multilayer nanoporous graphene membranes. The model features one free parameter, which is related to the excluded volume associated with the finite atomic size. We emphasize that this parameter is fixed for a given fluid (assuming a graphene membrane) and is not to be adjusted as a function of the pore radius. Our model is expected to extend to other two-dimensional nanoporous membranes made from similarly structured materials [1], such as MoS₂, hBN, etc.

The proposed model is found to be in excellent agreement with extensive MD simulation results for LJ fluids as well as low molecular weight hydrocarbons. One key to this result is to evaluate fluid properties such as viscosity and density at fluid conditions representative of those close to the pore entrance. The agreement extends to pore radii on the order of or even smaller than the characteristic size of the fluid atom/molecule, which is quite remarkable, given that the proposed model is based on continuum hydrodynamic concepts. This may be rationalized by noting that the

most important ingredient of the phenomena considered here, namely Sampson flow, is known for being particularly robust as the atomic size is reached. For a more extensive discussion the reader is referred to Ref. [27]. We also showed that with small modifications the proposed model can be generalized to describe the permeance of small, planar hydrocarbon molecules, such as benzene and xylenes for all pore radii, including the steric exclusion regime.

ACKNOWLEDGMENTS

We wish to acknowledge financial support from a Mathworks as well as an MIT Climate and Sustainability Consortium seed fund award. We also acknowledge the MIT SuperCloud and Lincoln Laboratory Supercomputing Center for providing computational resources that have contributed to the research results reported within this paper.

APPENDIX A: MOLECULAR SIMULATION SETUP FOR LJ FLUIDS

All MD simulations were performed using the LAMMPS software [48]. Nonbonded atomic interactions are modeled with the LJ potential

$$u_{ij} = 4\varepsilon_{ij} \left[\left(\frac{\sigma_{ij}}{r} \right)^{12} - \left(\frac{\sigma_{ij}}{r} \right)^6 \right], \quad (\text{A1})$$

where r is the distance between atoms i and j . Hereafter, subscripts c, h, and f are used to denote carbon, hydrogen, and fluid atoms, respectively. Quantities will be reported in nondimensional units using the characteristic distance σ_{ff} , the potential well depth ε_{ff} and the characteristic time $\tau = \sqrt{m_f \sigma_{ff}^2 / \varepsilon_{ff}}$, where m_f denotes the mass of the LJ particle.

The simulation geometry is shown in Fig. 2(a). The fluid, comprised of 24000 LJ fluid particles, is confined by two graphene sheets denoted as pistons, which also serve to impose a pressure difference between the two sides of the porous graphene membrane. The nanopore is created by removing carbon atoms; the pore edges were also terminated using hydrogen atoms. The nanopore radius falls within the range $0.65 \leq R \leq 5.9$; this measure represents the nominal pore radius defined as the distance between the pore center and the location of the centers of the hydrogen atom terminating the pore. The simulation domain is periodic in the plane of the membrane with dimensions $L_x = 23.6$ and $L_y = 22.9$. The height of the simulation domain is $L_z = 50.3$, where $z = 0$ denotes the membrane location.

Interaction parameters were taken to be $\varepsilon_{cc} = 0.0833$ and $\sigma_{cc} = 1$ for carbon atoms and $\varepsilon_{hh} = 0.0357$ and $\sigma_{hh} = 0.6817$ for hydrogen atoms. The membrane morphology was preserved by using a harmonic force field to describe bonded interactions, including C-C and C-H bonds, as well as C-C-H angles. The parameters for these bonded interactions are obtained from the CHARMM force field [46]; however, to accelerate the simulation, we have omitted the Urey-Bradley term in the angle potential. We examine three pairs of fluid-solid interaction strengths: weak $(\varepsilon_{cf}, \varepsilon_{hf}) = (0.0096, 0.0063)$, moderate $(\varepsilon_{cf}, \varepsilon_{hf}) = (0.0962, 0.0630)$, and strong $(\varepsilon_{cf}, \varepsilon_{hf}) = (0.2887, 0.1890)$, while holding σ_{cf} and σ_{hf} equal to 1 and 0.8409, respectively. In the interest of brevity, these parameter combinations will be referred to as $E = 0$, $E = 1$, and $E = 2$, respectively.

Simulations start in the NVT ensemble at a reduced temperature $T = 1.18$ and reduced fluid density $\rho = 0.76$; the fluid viscosity at these conditions is $\mu = 1.60$. Following an equilibration period of duration $\tau_{\text{relax1}} = 200$ under these conditions, external forces are applied to the piston graphene sheets to produce a pressure difference of 0.04 for pores with $R > 1.4$ and 0.4 for pores with $R < 1.4$. During this simulation phase the fluid evolves under NVE dynamics. Permeance data is collected following an equilibration period of duration $\tau_{\text{relax2}} = 1400$. This pressure difference was chosen to balance the need for flow velocities small enough for nonlinear effects to be negligible, but large enough for resolving the velocity profile in the pore [49]—the most sensitive to noise of the measured quantities—to acceptable statistical uncertainty levels.

The membrane permeance is calculated from the net number of fluid molecules crossing from the high- to the low-pressure reservoir over a period of $\tau_{\text{run}} = 60000$. The velocity profile is obtained by partitioning the region $-0.07 < z < 0.07$ into a series of concentric rings, each with a width of 0.42, and then averaging the fluid atomic velocities in the z direction within each ring.

Simulation results relating the potential repulsive core to the effective radius (see Fig. 3) were obtained using the potential

$$u_{\text{wf}} = 4\epsilon_{\text{wf}} \left[\left(\frac{\sigma_{\text{wf}}}{r - \Delta} \right)^{12} - \left(\frac{\sigma_{\text{wf}}}{r - \Delta} \right)^6 \right], \quad (\text{A2})$$

where subscript w refers to the wall atom.

APPENDIX B: MOLECULAR SIMULATION SETUP FOR ORGANIC LIQUIDS

All interactions involving the graphene membrane and organic molecules are described using the CHARMM force field [46], which has undergone parameter optimization for organic ligands. The simulation domain had dimensions of $83 \times 81 \times 280 \text{ \AA}^3$. The geometry of the nanoporous graphene membrane and simulation procedures follow those described above for LJ fluids.

Simulations were performed at $T = 300 \text{ K}$, using a pressure difference of $\Delta P = 200 \text{ bar}$. The simulation timestep was 1.3 fs. Due to the low permeance of organic molecules, the sampling period was at least 75 ns. A total of 3000 liquid molecules were simulated in each case. The viscosity of each liquid was determined through additional off-line simulations using the procedure of Ref. [50]. In these latter simulations, the total number of molecules exceeded 5000, with pressure controlled at 200 bar and a simulation time exceeding 10 ns. The viscosity of *o*-xylene, *p*-xylene, benzene, *n*-octane, and *i*-octane was calculated to be 0.86 ± 0.03 , 0.72 ± 0.04 , 0.62 ± 0.02 , 0.74 ± 0.05 , and $0.69 \pm 0.02 \text{ mPa s}$, respectively, in good agreement with experimental values [51,52].

-
- [1] L. Wang, M. S. Boutilier, P. R. Kidambi, D. Jang, N. G. Hadjiconstantinou, and R. Karnik, Fundamental transport mechanisms, fabrication and potential applications of nanoporous atomically thin membranes, *Nature Nanotechnol.* **12**, 509 (2017).
 - [2] X. Li, Y. Mo, W. Qing, S. Shao, C. Y. Tang, and J. Li, Membrane-based technologies for lithium recovery from water lithium resources: A review, *J. Membr. Sci.* **591**, 117317 (2019).
 - [3] S. P. Dharupaneedi, S. K. Nataraj, M. Nadagouda, K. R. Reddy, S. S. Shukla, and T. M. Aminabhavi, Membrane-based separation of potential emerging pollutants, *Sep. Purif. Technol.* **210**, 850 (2019).
 - [4] M. S. Boutilier, D. Jang, J.-C. Idrobo, P. R. Kidambi, N. G. Hadjiconstantinou, and R. Karnik, Molecular sieving across centimeter-scale single-layer nanoporous graphene membranes, *ACS Nano* **11**, 5726 (2017).
 - [5] S. Zhang, L. Shen, H. Deng, Q. Liu, X. You, J. Yuan, Z. Jiang, and S. Zhang, Ultrathin membranes for separations: A new era driven by advanced nanotechnology, *Adv. Mater.* **34**, 2108457 (2022).
 - [6] Y. Han, Z. Xu, and C. Gao, Ultrathin graphene nanofiltration membrane for water purification, *Adv. Funct. Mater.* **23**, 3693 (2013).
 - [7] A. Raza, J. Z. Hassan, A. Mahmood, W. Nabgan, and M. Ikram, Recent advances in membrane-enabled water desalination by 2d frameworks: Graphene and beyond, *Desalination* **531**, 115684 (2022).
 - [8] M. S. Boutilier, C. Sun, S. C. O'Hern, H. Au, N. G. Hadjiconstantinou, and R. Karnik, Implications of permeation through intrinsic defects in graphene on the design of defect-tolerant membranes for gas separation, *ACS Nano* **8**, 841 (2014).
 - [9] C. Sun, B. Wen, and B. Bai, Recent advances in nanoporous graphene membrane for gas separation and water purification, *Sci. Bull.* **60**, 1807 (2015).

- [10] D. Cohen-Tanugi and J. C. Grossman, Nanoporous graphene as a reverse osmosis membrane: Recent insights from theory and simulation, *Desalination* **366**, 59 (2015).
- [11] H. Qiu, W. Zhou, and W. Guo, Nanopores in graphene and other 2d materials: A decade's journey toward sequencing, *ACS Nano* **15**, 18848 (2021).
- [12] Z. Yuan, A. Govind Rajan, G. He, R. P. Misra, M. S. Strano, and D. Blankschtein, Predicting gas separation through graphene nanopore ensembles with realistic pore size distributions, *ACS Nano* **15**, 1727 (2021).
- [13] C. Sun, R. Zhou, Z. Zhao, and B. Bai, Nanoconfined fluids: What can we expect from them? *J. Phys. Chem. Lett.* **11**, 4678 (2020).
- [14] Y. Yang, X. Yang, L. Liang, Y. Gao, H. Cheng, X. Li, M. Zou, R. Ma, Q. Yuan, and X. Duan, Large-area graphene-nanomesh/carbon-nanotube hybrid membranes for ionic and molecular nanofiltration, *Science* **364**, 1057 (2019).
- [15] J. Buchheim, K.-P. Schlichting, R. M. Wyss, and H. G. Park, Assessing the thickness–permeation paradigm in nanoporous membranes, *ACS Nano* **13**, 134 (2019).
- [16] L. Cao, Q. Wen, Y. Feng, D. Ji, H. Li, N. Li, L. Jiang, and W. Guo, On the origin of ion selectivity in ultrathin nanopores: Insights for membrane-scale osmotic energy conversion, *Adv. Funct. Mater.* **28**, 1804189 (2018).
- [17] R. Castro-Muñoz, K. V. Agrawal, Z. Lai, and J. Coronas, Towards large-scale application of nanoporous materials in membranes for separation of energy-relevant gas mixtures, *Sep. Purif. Technol.* **308**, 122919 (2023).
- [18] D. S. Sholl and R. P. Lively, Seven chemical separations to change the world, *Nature (London)* **532**, 435 (2016).
- [19] R. P. Lively and D. S. Sholl, From water to organics in membrane separations, *Nature Mater.* **16**, 276 (2017).
- [20] R. P. Lively, The refinery of today, tomorrow, and the future: A separations perspective, *AIChE J.* **67**, e17286 (2021).
- [21] N. G. Hadjiconstantinou, The limits of Navier-Stokes theory and kinetic extensions for describing small-scale gaseous hydrodynamics, *Phys. Fluids* **18**, 111301 (2006).
- [22] C. Sun, M. S. Boutilier, H. Au, P. Poesio, B. Bai, R. Karnik, and N. G. Hadjiconstantinou, Mechanisms of molecular permeation through nanoporous graphene membranes, *Langmuir* **30**, 675 (2014).
- [23] N. Kavokine, R. R. Netz, and L. Bocquet, Fluids at the nanoscale: From continuum to subcontinuum transport, *Annu. Rev. Fluid Mech.* **53**, 377 (2021).
- [24] N. G. Hadjiconstantinou, Molecular mechanics of liquid and gas slip flow, *Annu. Rev. Fluid Mech.* **56**, 435 (2024).
- [25] R. A. Sampson, Xii. On Stokes's current function, *Philos. Trans. R. Soc. London, A* **182**, 449 (1891).
- [26] M. Suk and N. R. Aluru, Molecular and continuum hydrodynamics in graphene nanopores, *RSC Adv.* **3**, 9365 (2013).
- [27] S. Gravelle, L. Joly, C. Ybert, and L. Bocquet, Large permeabilities of hourglass nanopores: From hydrodynamics to single file transport, *J. Chem. Phys.* **141**, 18C526 (2014).
- [28] M. R. Hasan and B. H. Kim, Molecular transportation phenomena of simple liquids through a nanoporous graphene membrane, *Phys. Rev. E* **102**, 033110 (2020).
- [29] M. Heiranian and N. R. Aluru, Nanofluidic transport theory with enhancement factors approaching one, *ACS Nano* **14**, 272 (2020).
- [30] M. Heiranian, A. Taqieddin, and N. R. Aluru, Revisiting Sampson's theory for hydrodynamic transport in ultrathin nanopores, *Phys. Rev. Res.* **2**, 043153 (2020).
- [31] C. Sun, R. Zhou, Z. Zhao, and B. Bai, Extending the classical continuum theory to describe water flow through two-dimensional nanopores, *Langmuir* **37**, 6158 (2021).
- [32] J. A. Hossain and B. Kim, Scale effect on simple liquid transport through a nanoporous graphene membrane, *Langmuir* **37**, 6498 (2021).
- [33] J. A. Hossain and B. Kim, The validity of the continuum modeling limit in a single pore flows to the molecular scale, *Phys. Chem. Chem. Phys.* **25**, 24919 (2023).

- [34] G. J. Wang and N. G. Hadjiconstantinou, Why are fluid densities so low in carbon nanotubes? *Phys. Fluids* **27**, 052006 (2015).
- [35] Z. Dagan, S. Weinbaum, and R. Pfeffer, An infinite-series solution for the creeping motion through an orifice of finite length, *J. Fluid Mech.* **115**, 505 (1982).
- [36] K. Falk, F. Sedlmeier, L. Joly, R. R. Netz, and L. Bocquet, Molecular origin of fast water transport in carbon nanotube membranes: Superlubricity versus curvature dependent friction, *Nano Lett.* **10**, 4067 (2010).
- [37] S. K. Kannam, B. Todd, J. S. Hansen, and P. J. Davis, Slip flow in graphene nanochannels, *J. Chem. Phys.* **135**, 144701 (2011).
- [38] S. K. Kannam, B. Todd, J. S. Hansen, and P. J. Davis, Slip length of water on graphene: Limitations of non-equilibrium molecular dynamics simulations, *J. Chem. Phys.* **136**, 024705 (2012).
- [39] B. Radha, A. Esfandiari, F. Wang, A. Rooney, K. Gopinadhan, A. Keerthi, A. Mishchenko, A. Janardanan, P. Blake, L. Fumagalli *et al.*, Molecular transport through capillaries made with atomic-scale precision, *Nature (London)* **538**, 222 (2016).
- [40] Y. Xie, L. Fu, T. Niehaus, and L. Joly, Liquid-solid slip on charged walls: The dramatic impact of charge distribution, *Phys. Rev. Lett.* **125**, 014501 (2020).
- [41] Q. Xie, M. A. Alibakhshi, S. Jiao, Z. Xu, M. Hempel, J. Kong, H. G. Park, and C. Duan, Fast water transport in graphene nanofluidic channels, *Nature Nanotechnol.* **13**, 238 (2018).
- [42] J. Abraham, K. S. Vasu, C. D. Williams, K. Gopinadhan, Y. Su, C. T. Cherian, J. Dix, E. Prestat, S. J. Haigh, I. V. Grigorieva *et al.*, Tunable sieving of ions using graphene oxide membranes, *Nature Nanotechnol.* **12**, 546 (2017).
- [43] G. J. Wang and N. G. Hadjiconstantinou, Universal molecular-kinetic scaling relation for slip of a simple fluid at a solid boundary, *Phys. Rev. Fluids* **4**, 064201 (2019).
- [44] C. Sendner, D. Horinek, L. Bocquet, and R. R. Netz, Interfacial water at hydrophobic and hydrophilic surfaces: Slip, viscosity and diffusion, *Langmuir* **25**, 10768 (2009).
- [45] N. G. Hadjiconstantinou and M. M. Swisher, On the equivalence of nonequilibrium and equilibrium measurements of slip in molecular dynamics simulations, *Phys. Rev. Fluids* **7**, 114203 (2022).
- [46] S. Jo, T. Kim, V. G. Iyer, and W. Im, CHARMM-GUI: A web-based graphical user interface for CHARMM, *J. Comput. Chem.* **29**, 1859 (2008).
- [47] National Center for Biotechnology Information, <https://pubchem.ncbi.nlm.nih.gov>.
- [48] A. P. Thompson, H. M. Aktulga, R. Berger, D. S. Bolintineanu, W. M. Brown, P. S. Crozier, P. J. in 't Veld, A. Kohlmeyer, S. G. Moore, T. D. Nguyen, R. Shan, M. J. Stevens, J. Tranchida, C. Trott, and S. J. Plimpton, LAMMPS - a flexible simulation tool for particle-based materials modeling at the atomic, meso, and continuum scales, *Comput. Phys. Commun.* **271**, 108171 (2022).
- [49] N. G. Hadjiconstantinou, A. L. Garcia, M. Z. Bazant, and G. He, Statistical error in particle simulations of hydrodynamic phenomena, *J. Comput. Phys.* **187**, 274 (2003).
- [50] A. T. Celebi, C. T. Nguyen, R. Hartkamp, and A. Beskok, The role of water models on the prediction of slip length of water in graphene nanochannels, *J. Chem. Phys.* **151**, 174705 (2019).
- [51] X. Meng, X. Gu, J. Wu, and V. Vesovic, Viscosity measurements of ortho-xylene, meta-xylene, para-xylene and ethylbenzene, *J. Chem. Thermodyn.* **95**, 116 (2016).
- [52] F. V. dos Santos and C. N. De Castro, Viscosity of toluene and benzene under high pressure, *Int. J. Thermophys.* **18**, 367 (1997).